

# Speckle Meth

## 23. Speckle Methods

Yimin Gan, Wolfgang Steinchen (deceased)

Speckle methods, which are based on the well-known speckle effect, play an important role in experimental mechanics. The formation and some important properties of speckle pattern are introduced firstly. Dealing with changes in surface intensity and positions of speckle patterns, speckle methods can be grouped into speckle interferometry and speckle correlation. The basic concepts and evaluations of speckle interferometry and speckle correlation are reviewed. Shearography, a special class of speckle interferometry suitable for measurement in the field (e.g., industrial applications), is introduced and used as a representative method for strain measurement and nondestructive testing (NDT).

23.1	<b>Laser Speckle</b> .....	655
23.1.1	Laser Speckle Phenomenon .....	655
23.1.2	Some Properties of Speckles .....	656
23.2	<b>Speckle Metrology</b> .....	658
23.2.1	Speckle Correlation .....	658
23.2.2	Speckle Interferometry .....	660
23.2.3	Shearography .....	662
23.2.4	Quantitative Evaluation (SI) .....	665
23.3	<b>Applications</b> .....	668
23.3.1	NDT/NDE .....	668
23.3.2	Strain Measurement .....	670
23.4	<b>Bibliography</b> .....	672
	<b>References</b> .....	672

Speckle pattern is an interference phenomenon which has been investigated since the time of Newton. The earliest observation of the phenomenon of speckling appears to have been by *Exner* [23.1], nearly a century ago, in connection with a study of the Fraunhofer rings formed when a beam of coherent light is diffracted by a number of particles of the same size distributed at random [23.2]. A photograph of the Fraunhofer rings covered with a speckle pattern was first pub-

lished by *von Laue* [23.3], who also worked out the first- and second-order speckle probability density functions.

A noisy, random granular speckle pattern is also a carrier of important information. The first metrological application using a speckle pattern was published by *Groh* [23.4] in 1970. Today, speckle metrology is an important and rapidly growing area of optical metrology in experimental mechanics.

### 23.1 Laser Speckle

#### 23.1.1 Laser Speckle Phenomenon

When a temporally and spatially coherent laser beam is incident on a surface that is optically rough (with a surface roughness  $R_z$  that is greater than the laser wavelength  $\lambda$ ), the microscopic small waves of the scattered light obtain a different phase relative to the phase of the incident wave. The dephased, but still coher-

ent wavelets interfere constructively (in antiphase) or destructively (in equiphase) in space and generate a statistically distributed, granular spatial speckle pattern. Such granular patterns can also be observed for optically rough surfaces illuminated by much less coherent light, e.g., mercury lamp and laser diode.

According to the experimental setup, speckles can be divided into two categories: objective and subjec-

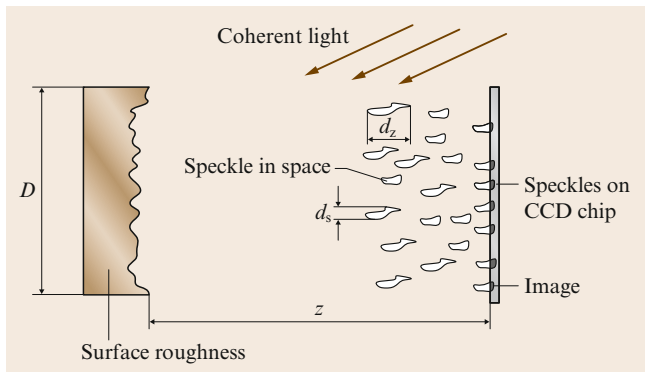


**Fig. 23.1** Formation of objective speckles in free space

tive speckles. Laser speckles existing in free space are known as objective or far-field speckles (Fig. 23.1). When an imaging system is used to observe speckle, the recorded information is known as a subjective speckle pattern (Fig. 23.2), in which case the properties depend on the imaging system. Subjective speckles are formed by the superposition of complex amplitudes of scattered wavelets in the image plane. Each point of the image plane registers only light beams which are reflected by the illuminated part of the object surface. Therefore they depend on the scattered light collected by the image aperture, and the speckle size is determined by the spatial frequencies passed through the lens system [23.5]. An observer who looks at the object surface perceives the subjective speckle effect because the human eye has a similar aperture and lens optics. Usually the speckle pattern in speckle metrology is observed and recorded by an optical system similar to that shown in Fig. 23.2 and the subjective or image speckles are simply called speckles.

### 23.1.2 Some Properties of Speckles

#### Statistical Intensity Distribution

Stochastic spatially distributed speckles are best described quantitatively by probability and statistics [23.6]. A laser emits linearly polarized light, but the direction of preference becomes lost when the rays are reflected by an optically rough surface. When the intensity field incident at the point  $P(x, y, z)$  on the object surface is perfectly monochromatic and perfectly polarized, the field is then represented by the following signal:

$$U(x, y, z, t) = A(x, y, z) \exp[i(2\pi ft)], \quad (23.1)$$

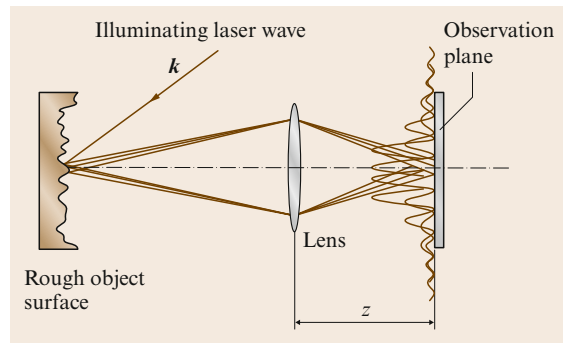


**Fig. 23.2** Formation of subjective speckle patterns

where  $f$  is the optical frequency and  $A(x, y, z)$  is the complex phasor amplitude. The directly observable magnitude is the intensity at  $P(x, y, z)$ , which is given by

$$\begin{aligned} I(x, y, z) &= \lim_{T_f \rightarrow \infty} \frac{1}{T_f} \int_{-T_f/2}^{+T_f/2} |U(x, y, z; t)|^2 dt \\ &= |a(x, y, z)|^2, \end{aligned} \quad (23.2)$$

where  $T_f$  is the exposure time. The complex phasor amplitude at point  $P(x, y, z)$  of the surface can be described mathematically as

$$A(x, y, z) = \sum_{k=1}^N |a_k| e^{i\Phi_k}, \quad (23.3)$$

where  $a_k$  is the amplitude and  $\Phi_k$  is the phase of the  $k$ -th scattered elementary wave. In a fully developed

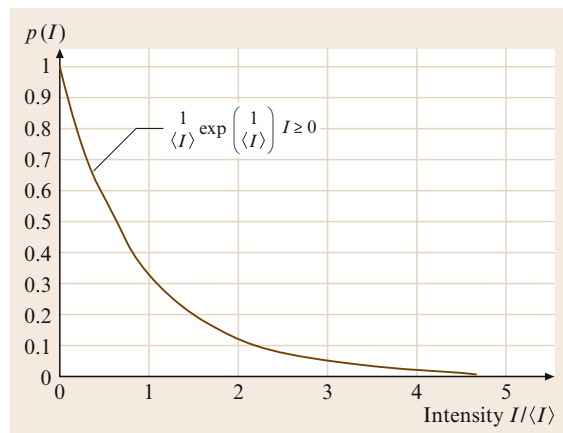


**Fig. 23.3** Probability density function based on numerous measurements taken from a speckle pattern

speckle pattern  $a_k$  and  $\Phi_k$  are statistically independent of each other and the phase  $\Phi_k$  is uniformly distributed between  $-\pi$  and  $+\pi$ . The complex amplitude of the speckle pattern obeys circular Gaussian statistics in the complex plane. The resulting intensity of the speckle pattern has a negative exponential probability distribution given by

$$p(I) = \frac{1}{\langle I \rangle} \exp\left(\frac{-I}{\langle I \rangle}\right) \quad I \geq 0, \quad (23.4)$$

where  $\langle I \rangle$  is the mean value [23.6]. The negative exponential distribution  $p(I)$  (Fig. 23.3) establishes that the intensity  $I$  of the point  $P(x, y, z)$  lies between  $I$  and  $I + dI$ . The most probable intensity of the speckle distribution in the image plane is zero. The contrast  $\gamma$  of the speckle pattern is defined as  $\gamma = \sigma/\langle I \rangle$ . Because the standard deviation  $\sigma$  and the mean value  $\langle I \rangle$  are identical, a speckle pattern which shows a good contrast.

The speckle intensity and speckle phase are the quantities in speckle interferometry from which displacement, strain, surface roughness etc. are derived by means of first-order statistics. The second-order statistics of the scattered field contains the description of the spatial structure of the speckle field.

### Speckle Size

The scattered wavefront from the neighboring points  $P_1$  and  $P_2$  of the object surface are phase shifted as a result of the *chain of hills and valleys* created by its roughness, and the conjugated image points in the observation plane are  $P'_1$  and  $P'_2$ . Each image point yields an intensity field, as shown in Fig. 23.4, for a diffraction restricted by the point-spread function (PSF). The Fraunhofer diffraction function  $I = I_0 \{2J_1[2\pi a \sin(\alpha)/\lambda][2\pi a \sin(\alpha)/\lambda]\}^2$  yields the intensity of the Airy disk for perpendicular incidence, where  $a = d_{Ap}/2$ ,  $\alpha$  is the angle of the diffracted light deviating from the normal direction, and  $J_1$  is the Bessel function of first order. The phase shift of the intensity distributions is caused by a difference in the light waves; when the neighboring point-spread functions are overlapping, constructive or destructive interference is formed (i.e., microscopic interference). The overlapping region caused by the diffraction of the aperture plate is determined by the diameter of the aperture  $d_{Ap}$ , which is on the order of the size of Airy disk and corresponds to the diameter of the speckle  $d_s$  (23.5) where  $f$  is the distance from the lens to the image plane [23.7]. The diameter of the first dark ring observed at the

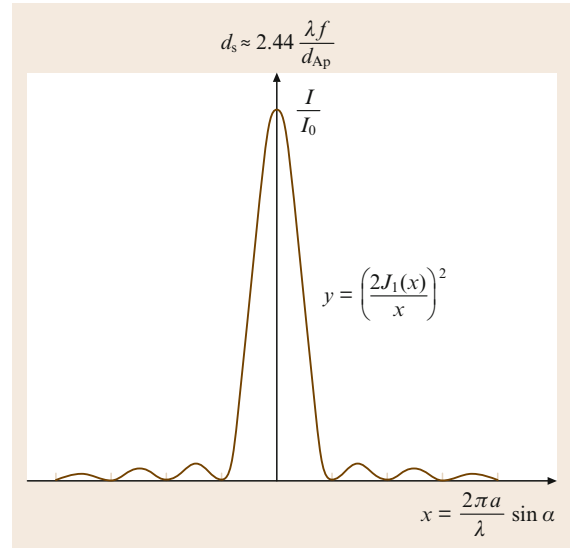


**Fig. 23.4** Intensity distribution varying with the diffraction order of a plane wave through a circular aperture

diffraction angle  $\Phi \approx 1.22\lambda/2r$  within the boundary of resolution is given by

$$d_s \approx 2.44 \frac{\lambda f}{d_{Ap}}. \quad (23.5)$$

In most imaging systems, the  $F$ -number  $F = f/d_{Ap}$  and the laser wavelength  $\lambda$  are known quantities. The speckle size increases with increasing  $F$ -number and laser wavelength. This characteristic of the subjective speckles is useful because the speckle size can be adjusted by the aperture lens for different measuring problem requirements [23.7–10].

Speckle size can also be extracted using an autocorrelation function, as described by *Goodman* [23.5]. The results of both methods are identical.

### Definiteness of Laser Speckles

The speckles, which are randomly distributed in space, are irregularly shaped. The speckle pattern, however, is temporally constant and spatially determined. Each surface structure generates its own speckle pattern or wavefront in space. Thus, the speckle pattern provides a *fingerprint* of the illuminated area for the microstructure. When the microstructure of the object surface is changed due to movement or deformation, the observed speckle pattern changes accordingly. Because of this property, the speckle pattern can be used as a tool for metrological applications.

## 23.2 Speckle Metrology

A single speckle pattern contains information about the surface microstructure. However, it is not possible to deduce the phase information from this individual interferogram. At least two speckle patterns belonging to the same surface structure are required to compare separate states of deformation. A comparison of the two speckle patterns obtained from the object surface provides two sets of information: a change in the surface geometry and a change in the surface intensity distribution. A speckle pattern experiences both changes simultaneously. However, for many applications these changes can be studied separately. Measuring techniques dealing with changes in surface intensity are grouped under speckle interferometry (SI) and those dealing with geometric changes are grouped under speckle correlation (SC).

### 23.2.1 Speckle Correlation

When positional shifting between two speckle patterns in the image plane is studied, the method is known as speckle photography (SP) or speckle correlation (SC). These techniques were developed around 1968 by *Burch and Tokarski* [23.11]. *Archbold and Ennos* [23.12] recorded two states (before and after loading) of an object surface illuminated with an expanded laser beam on a single photographic plate. When the specklegram developed by this process is illuminated by a narrow laser beam, Young's fringes result in the far field; their frequency carries information about the displacement between the two exposures.

Recently, speckle patterns have been recorded digitally by charge-coupled device (CCD) sensors and stored in separate frames. Figure 23.5 shows the experimental setup. The displacement field can be determined numerically using a two-dimensional cross-correlation

algorithm. Digital speckle correlation (DSC), also known as digital speckle photography (DSP), is much faster and easier to use than conventional SC because there is no need for film development or additional processing for reconstruction.

#### Principles of Digital Speckle Correlation (DSC)

In DSC the two speckle patterns  $I$  and  $I'$  acquired before and after deformation are usually divided into a set of subimages. The cross-correlation algorithm does not track the position change of each speckle, but rather the movement of a number of speckles acting together as a subimage. The correlation function is calculated for each pair of corresponding subimages and the respective displacement is derived from the position of the maximum.

Figure 23.6 schematically illustrates the principle of calculating the displacement field. A subimage  $A$  in image  $I$  is allowed to sweep over the image  $I'$ . When an area is found where the statistical agreement (cross-correlation) is highest, this area is labeled as subimage  $A'$  and is considered to correspond to subimage  $A$ . The discrete cross-correlation between  $A$  and  $A'$  can be calculated as

$$R_{AA'}(d_x, d_y) = \frac{1}{NM} \sum_{i=0}^{N-1} \sum_{j=0}^{M-1} A(i, j) A'(i + d_x, j + d_y); \quad (23.6)$$

the discrete normalized cross-covariance is defined as

$$r_{AA'}(d_x, d_y) = \frac{R_{AA'} - \bar{A}\bar{A}'}{\sigma_A\sigma_{A'}}, \quad (23.7)$$

where  $d_x$  and  $d_y$  are displacements in the  $x$ - and  $y$ -directions, respectively.

$$\bar{A} = \frac{1}{NM} \sum_{i=0}^N \sum_{j=0}^M A(i, j) \quad \text{and}$$

$$\bar{A}' = \frac{1}{NM} \sum_{i=0}^N \sum_{j=0}^M A'(i + d_x, j + d_y)$$

are the mean values of subimages  $A$  and  $A'$ .

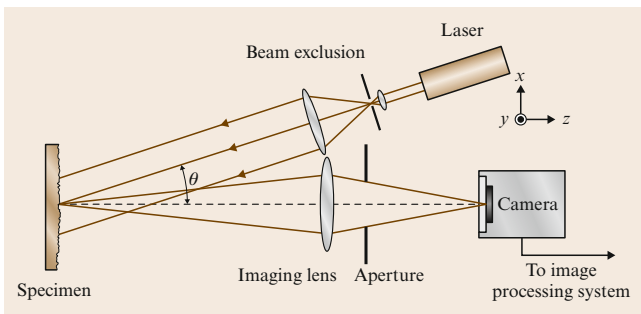
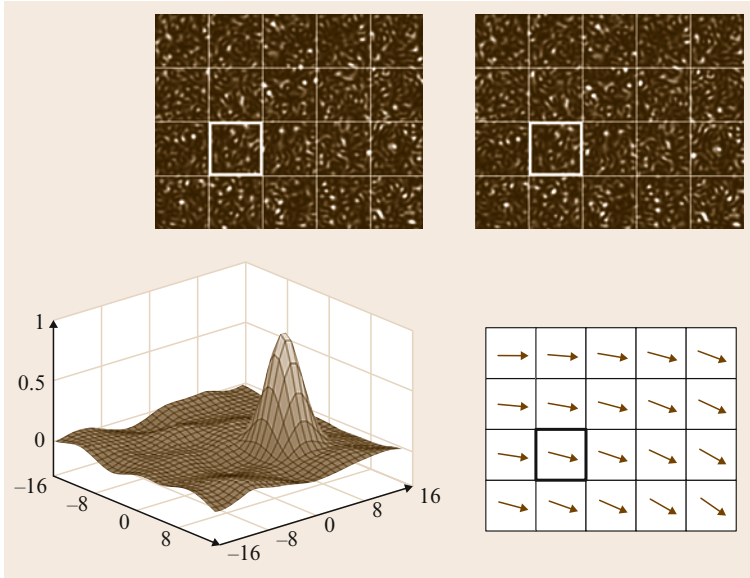


Fig. 23.5 The experimental setup for digital speckle correlation



**Fig. 23.6** Principle of displacement field measurement [23.13]

$\sigma_A$  and  $\sigma_{A'}$  are the variances of  $A$  and  $A'$  and can be calculated as

$$\sigma_A^2 = \frac{1}{NM} \sum_{i=0}^N \sum_{j=0}^M A^2(i, j) - \bar{A}^2 \quad \text{and}$$

$$\sigma_{A'}^2 = \frac{1}{NM} \sum_{i=0}^N \sum_{j=0}^M A'^2(i, j) - \bar{A}'^2.$$

The movement over the surface from position  $A$  to  $A'$  is found by the position of the correlation peak and is given by the displacement vector of the midpoint of subimage  $A$ . These calculations are done for all subimages of  $I$  until a displacement field of the whole surface is obtained, meaning that the movement is determined in two directions,  $x$  and  $y$ . The height of the correlation peak indicates how similar the cross-correlated subimages are and hence yields a value of the accuracy of the measurement.

Usually, the complete cross-correlation function is required and the direct calculation by (23.7) is rather time consuming. It is much more efficient to perform the cross-correlation in the Fourier domain by using a fast Fourier transform (FFT) algorithm. In virtue of the Wiener–Khinchine theorem [23.13], the cross-correlation is the Fourier transform of the cross-power spectrum which can be calculated as

$$R_{AA'}(d_x, d_y) = FT^{-1}[FT(A) * FT(A')], \quad (23.8)$$

where  $FT$  and  $FT^{-1}$  are the discrete Fourier transform and its inverse, respectively. The asterisk denotes the complex conjugate. The procedure is illustrated in Fig. 23.7.

The size limitation of the object being studied depends mainly on the magnification of the imaging system. The accuracy of the correlation technique is about 1% of the pixel pitch (i. e., it depends on the size of the studied area, the magnification, and the number of pixels of the detector). If the object being studied is small, smaller displacements can be determined than if the same detector were used to study a larger object. A drawback with this method is that the images are divided into subimages, thereby lowering the spatial resolution. The larger the the size of subimages, the lower the resolution.

Using the conventional imaging geometry of SC the three-dimensional deformation can be obtained from a pair of images by the tilt of an object  $\gamma$  against the starting position, i. e., the gradient of the out-of-plane deformation determined from corresponding subimages with a subsequent integration over the whole image (Fig. 23.2). The tilt can be calculated from the frequency dependence of the two correlating speckle pattern [23.13].

#### White-Light Speckle Correlation

The deformation or movement of an object can be detected by calculating the positional changes of two speckle patterns according to two object states using

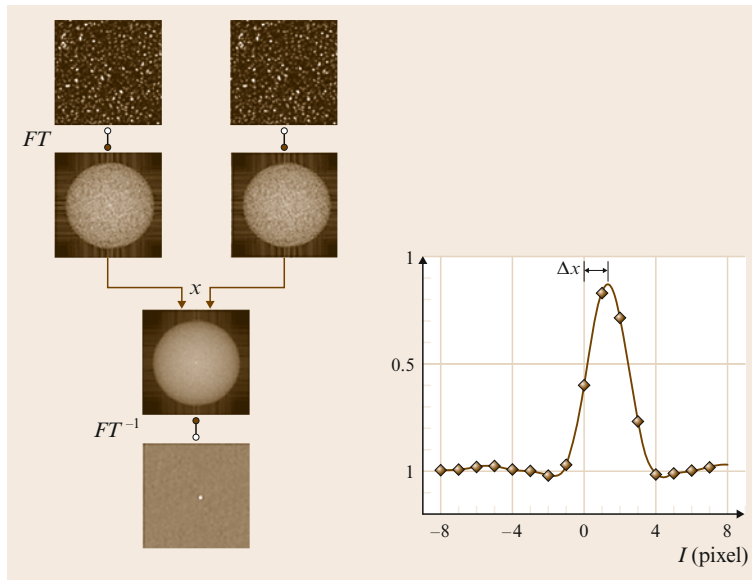


**Fig. 23.7** Flow chart of the correlation algorithm using Fourier transformation [23.13]

**DSC.** Actually, speckle patterns need not be generated by laser; they can also be formed artificially. In practical applications the object surface is first painted matt white and then sprayed with black speckles. When the object surface is illuminated by white light, the image of the artificial speckle pattern looks like the image of a laser speckle pattern. Since the white-light speckle pattern is random, the cross-correlation algorithms can be used to determine the positional changes of the white-light speckle pattern due to object deformation or movement.

Since the artificial speckles are larger than the real laser speckles, white-light speckle correlation, which is

also called digital image correlation (**DIC**), is not as sensitive as laser speckle correlation (**SC**). The lower sensitivity of **DIC** can be a positive attribute, since it can be used in noisy conditions. More about this technique can be found in the chapter *Image Correlation* Chap. 20 in this Handbook.

### 23.2.2 Speckle Interferometry

An alternative speckle measuring technique is speckle interferometry (**SI**). Unlike the speckle correlation, which measures the positional changes of speckles, the

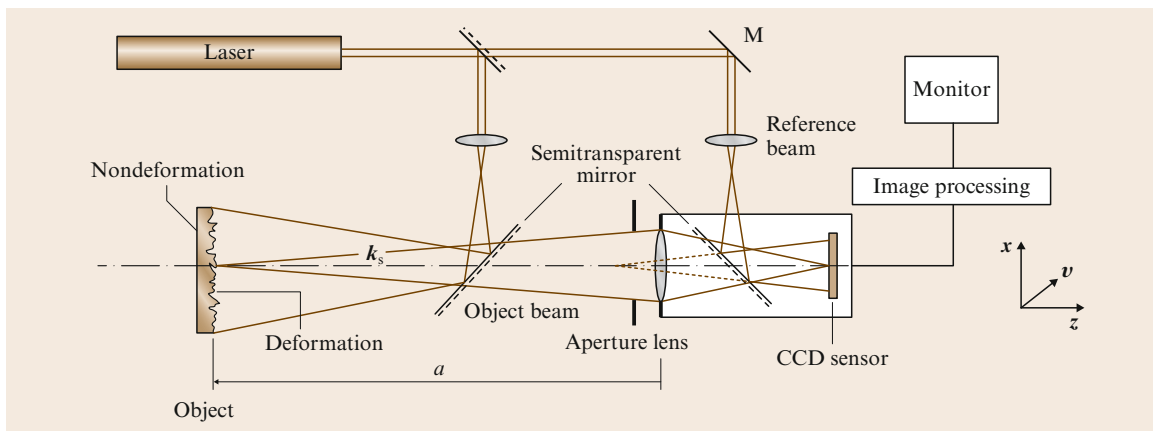


**Fig. 23.8** Speckle interferometer for measuring the displacements of the object which occur mainly in the direction vertical to the surface of the object

phase changes carried by intensity changes of speckles are studied in speckle interferometry.

### Principles of Speckle Interferometry

A schematic setup of a speckle interferometer is shown in Fig. 23.8. A reference beam and the object beam, which is scattered from the surface of the object, superimpose and generate an interfered speckle pattern in the image plane, which is known as a speckle interferogram. These speckle patterns therefore contain essential information about the random phase.

A point  $P(x, y)$  in the speckle interferogram can be expressed as a product of complex and conjugate complex terms by using

$$\begin{aligned} I &= (a_o e^{i\theta_o} + a_r e^{i\theta_r})(a_o e^{i\theta_o} + a_r e^{i\theta_r})^* \\ &= a_o^2 + a_r^2 + 2a_o a_r \cos(\theta_o - \theta_r) \\ &= a_o^2 + a_r^2 + 2a_o a_r \cos(\phi_{or}), \end{aligned} \quad (23.9)$$

where  $\phi_{or} = \theta_o - \theta_r$  is the random phase;  $a_o e^{i\theta_o}$  and  $a_r e^{i\theta_r}$  are a temporally constant object beam and reference beam, respectively; and  $a_o$ ,  $a_r$ , and  $\theta_o$ ,  $\theta_r$  are the amplitude and phase of the object beam and reference beam, respectively.

When the object is deformed, the interferogram changes due to the changes in the object wave. The intensity  $I'$  at the same point  $P$  in the interferogram after loading can be described as

$$\begin{aligned} I' &= a_o'^2 + a_r^2 + 2a_o' a_r \cos(\theta_o' - \theta_r) \\ &= a_o'^2 + a_r^2 + 2a_o' a_r \cos(\phi_{or} + \Delta) \\ &= a_o'^2 + a_r^2 + 2a_o' a_r \cos(\phi_{or}'), \end{aligned} \quad (23.10)$$

where  $\Delta = \phi_{or}' - \phi_{or}$  is the phase change between the two states. Since the change of the amplitude in the object wave can usually be neglected (i.e.,  $a_o \approx a_o'$ ), the difference between the intensities  $I$  and  $I'$  is only a phase change  $\Delta$ .

In classic speckle interferometry, two speckle patterns corresponding to the object before and after deformation of object are recorded on a single photographic plate. During reconstruction, the developed photographic plate is illuminated by the same reference beam to observe and evaluate the correlation fringes.

In recent speckle interferometry, which is also called electronic speckle pattern interferometry (ESPI), two speckle patterns are recorded by a CCD chip [or a complementary metal–oxide–semiconductor (CMOS) chip] separately and stored in a computer. The fringes can be generated numerically by digital subtraction and

can be observed in quasi real time. The intensity at a point  $P(x, y)$  can be interpreted as

$$\begin{aligned} I_s &= |I - I'| \\ &= 2a_o a_r |\cos(\phi_{or}) - \cos(\phi_{or} + \Delta)| \\ &= 4a_o a_r \left| \sin\left(\phi_{or} + \frac{\Delta}{2}\right) \sin\left(\frac{\Delta}{2}\right) \right|. \end{aligned} \quad (23.11)$$

The above equation represents a high-frequency carrier  $\sin(\phi + \Delta/2)$  modulated by a low-frequency factor  $\sin(\Delta/2)$ , which depends on small local deformations of the object due to loading.

If each speckle covers 1 pixel, the pixels will be black ( $I_s = 0$ ) when the intensity of both images are identical, namely  $\Delta = k2\pi$  ( $k = 0, 1, 2, 3, \dots$ ). The brightness of the pixel in the resulting image  $I_s$  will increase as the difference between the intensities  $I$  and  $I'$  increases. Pixels with the same brightness generate macroscopic lines (fringes) in the resulting image  $I_s$ .

### Fringe Interpretation

The visible fringes of an interferogram describe the distribution of relative phase changes. Figure 23.9 shows the geometric relation between the illumination vector  $\mathbf{k}_1$ , the observation vector  $\mathbf{k}_2$ , and the deformation vector of a point  $P$  on an object surface  $\mathbf{d}$ . The relative phase difference can be shown to be

$$\Delta = \mathbf{k}_2 \mathbf{d} - \mathbf{k}_1 \mathbf{d} = \mathbf{k}_s \mathbf{d}, \quad (23.12)$$

where  $\mathbf{k}_s = \mathbf{k}_2 - \mathbf{k}_1$  is called the sensitivity vector.

In  $x, y, z$ -coordinates, (23.12) can be expressed as

$$\Delta = \mathbf{k}_s (u\mathbf{e}_x + v\mathbf{e}_y + w\mathbf{e}_z) = u\mathbf{k}_s \mathbf{e}_x + v\mathbf{k}_s \mathbf{e}_y + w\mathbf{k}_s \mathbf{e}_z, \quad (23.13)$$

where  $u, v$ , and  $w$  are the components of the deformation vector and  $\mathbf{e}_x, \mathbf{e}_y$ , and  $\mathbf{e}_z$  are the unit vectors in the  $x$ -,  $y$ -, and  $z$ -directions, respectively. The sensitivity

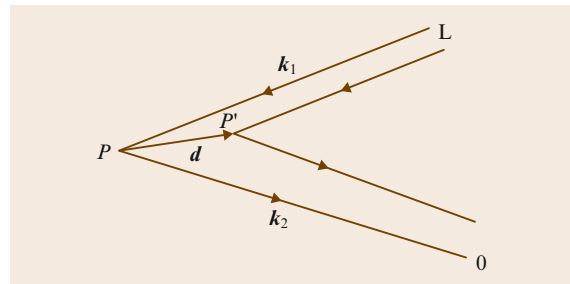
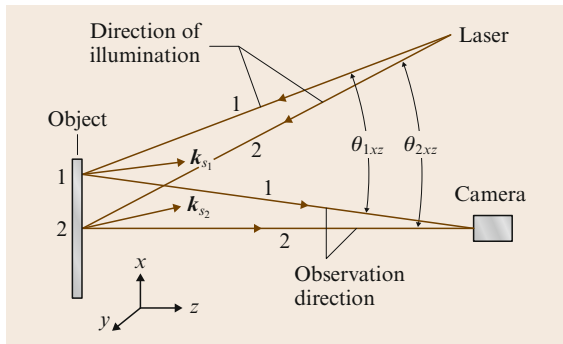


Fig. 23.9 Geometric relation of the light source  $L$ , observation position  $O$  and the object  $P$



**Fig. 23.10** Sensitivity vector and point of the object surface

vector  $\mathbf{k}_s$  lies along the bisector of the angle between the illumination and viewing directions and is theoretically not the same for each point of the object surface due to the changing illumination and observation directions (Fig. 23.10). However, it can be assumed that the sensitivity vector  $\mathbf{k}_s$  at each point of the investigated surface is equal when the dimensions of the object are small compared with the distances between the laser and the object or the camera and the object. To determine the sensitivity vector  $\mathbf{k}_s$ , the center point of the object is chosen (Fig. 23.11). Its magnitude can be expressed as

$$|\mathbf{k}_s| = (4\pi/\lambda) \cos(\theta_{xz}/2), \quad (23.14)$$

where  $\lambda$  is the wavelength of the laser light and  $\theta_{xz}$  is the angle between the illumination and observation vectors in the  $x, z$ -plane.

If the illumination and observation vectors are perpendicular to the object surface, namely  $\mathbf{k}_s \mathbf{e}_z = 1$  and  $\mathbf{k}_s \mathbf{e}_y = \mathbf{k}_s \mathbf{e}_x = 0$ , the relative phase difference is therefore

$$\Delta = \frac{4\pi}{\lambda} w. \quad (23.15)$$

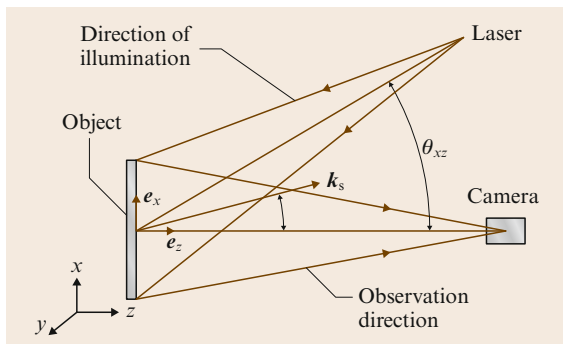


**Fig. 23.11** Simplified sensitivity vector  $\mathbf{k}_s$

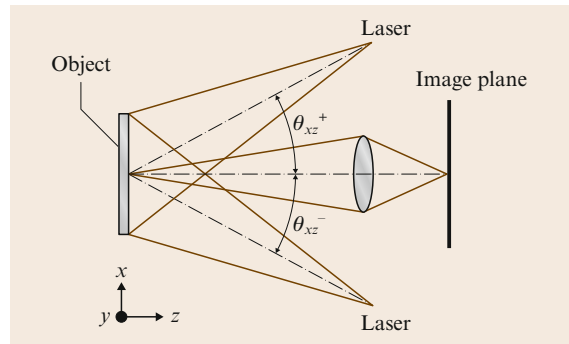


**Fig. 23.12** Optical arrangement for measuring in-plane displacement

Since only the out-of-plane displacement is measured, this kind of interferometer is known as an out-of-plane-sensitive interferometer.

For measuring in-plane displacements, the optical layout illustrated in Fig. 23.12 is often used. Two laser beams are arranged symmetrically on each side of the object with identical angles of incidence. The angle between the illumination vector and the observation vector is the same for both beams,  $\theta_{xz}^+ = \theta_{xz}^- = \theta$ . When the object is illuminated by two laser beams simultaneously, the relative phase change or the displacements in the  $x$ -direction can be written as

$$\begin{aligned} \Delta_{xz} = & \frac{2\pi}{\lambda} [u(\sin \theta_{xz}^+ + \sin \theta_{xz}^-) \\ & + w(\cos \theta_{xz}^+ - \cos \theta_{xz}^-)] = \frac{4\pi}{\lambda} u \sin \theta. \end{aligned} \quad (23.16)$$

The second in-plane displacement  $\Delta_{yz}$  can be measured similarly when both laser beams illuminate the object in the  $y, z$ -plane.

### 23.2.3 Shearography

Speckle pattern shearing interferometry (SPSI), which is more easily called shearography, was first investigated for direct measurement of the first derivative of deformation by *Leendertz* and *Butters* [23.14] and *Hung* [23.15]. Unlike other methods of speckle interferometry, e.g., *ESPI*, the interference in shearography is generated by two identical, laterally sheared object beams. This effect can be realized by a shear element which is located between the object and camera. Since no additional reference beam is needed, the setup for shearography is simple. Furthermore, compared with *ESPI*, shearography is relatively insensitive to distur-



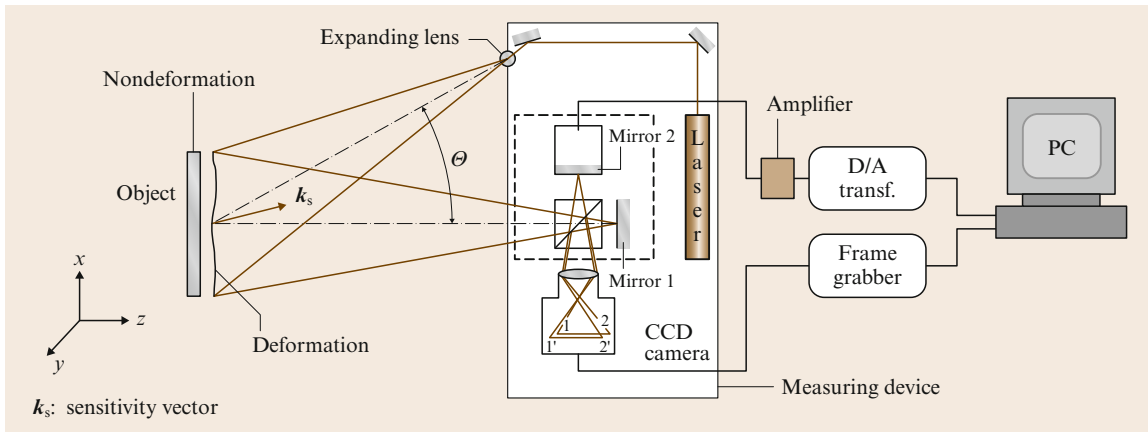


**Fig. 23.13** The experimental setup of digital shearography using single-beam illumination

bances from the environment and is very suitable for measurement under industrial conditions.

**Principle of Digital Shearography**

The experimental setup of digital shearography with single-beam illumination is shown in Fig. 23.13. The tested object is illuminated by an expanded laser beam. The light reflected from the object surface is focused on the image plane of an image CCD camera, where a modified Michelson interferometer is implemented in front of its lens instead of the optical shearing element. A pair of laterally sheared images of the tested object is generated on the image plane of the CCD camera by turning mirror 1 of the Michelson interferometer to a very small angle from the normal position. Two images with a certain shearing  $\delta$  interfere with each other and generate a shearing speckle pattern interferogram.

The rays from  $P_1 = P_1(x, y)$  on the object are mapped into two points  $P'_1 = P_1(x, y)$  and  $P''_1 = P'_1(x + \delta x', y)$  in the image plane (Fig. 23.14). Similarly, the point  $P_2 = P_2(x + \delta x', y)$  on the object surface is mapped to two points  $P'_2 = P'_2(x + \delta x', y)$  and  $P''_2 = P''_2(x + 2\delta x', y)$ , etc. At the point  $(x + \delta x', y)$  in the shearographic interferogram  $P'_2$  and  $P''_1$  are superposed. The intensity at this point can be expressed as:

$$\begin{aligned}
 I &= (a_1 e^{i\theta_1} + a_2 e^{i\theta_2})(a_1 e^{i\theta_1} + a_2 e^{i\theta_2})^* \\
 &= a_1^2 + a_2^2 + 2a_1 a_2 \cos(\theta_1 - \theta_2) \\
 &= a_1^2 + a_2^2 + 2a_1 a_2 \cos(\phi_{12}), \tag{23.17}
 \end{aligned}$$

where  $\phi_{12} = \theta_1 - \theta_2$  is the random phase, and  $a_1 e^{i\theta_1}$  and  $a_2 e^{i\theta_2}$  are temporally constant object beams from  $P_1$  and  $P_2$ , respectively. When the object is deformed, an optical path change occurs due to the surface displacement

of the object. This optical path change induces a relative phase change between the two interfering points. Thus, the intensity distribution of the speckle pattern is slightly altered and is mathematically represented by

$$\begin{aligned}
 I' &= (a_1 e^{i(\theta_1 + \Delta_1)} + a_2 e^{i(\theta_2 + \Delta_2)})(a_1 e^{i(\theta_1 + \Delta_1)} + a_2 e^{i(\theta_2 + \Delta_2)})^* \\
 &= a_1^2 + a_2^2 + 2a_1 a_2 \cos(\theta_1 - \theta_2 + \Delta_1 - \Delta_2) \\
 &= a_1^2 + a_2^2 + 2a_1 a_2 \cos(\phi_{12} + \Delta_{12}), \tag{23.18}
 \end{aligned}$$

where  $\Delta_{12} = \Delta_1 - \Delta_2$  is the relative phase difference between the two phase changes at points  $P_1$  and  $P_2$ .

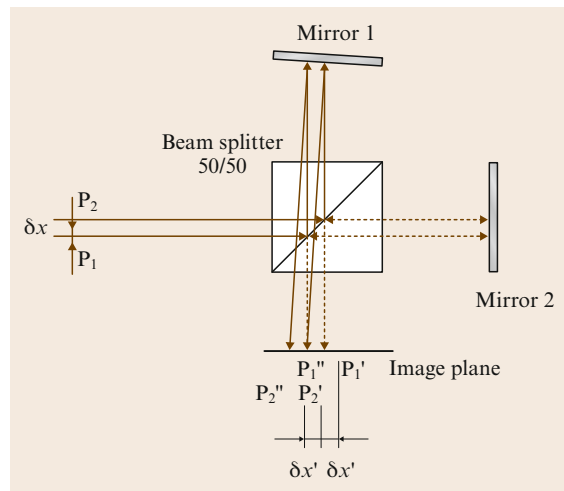


**Fig. 23.14** Schematic of shearing interferometry

Pixel-by-pixel digital subtraction of the two intensity distributions yields a macroscopic fringe pattern, (i. e., the shearogram or shearographic correlogram).

### Fringe Interpretation in Shearography

As mentioned earlier, in shearography the deformation derivatives can be measured directly. Using (23.13) the relative phase difference  $\Delta_{12}$  can be written as

$$\begin{aligned}\Delta_{12} &= \Delta_1 - \Delta_2 \\ &= u_1 \mathbf{k}_s \mathbf{e}_x + v_1 \mathbf{k}_s \mathbf{e}_y + w_1 \mathbf{k}_s \mathbf{e}_z \\ &\quad - u_2 \mathbf{k}_s \mathbf{e}_x + v_2 \mathbf{k}_s \mathbf{e}_y + w_2 \mathbf{k}_s \mathbf{e}_z \\ &= \delta u \mathbf{k}_s \mathbf{e}_x + \delta v \mathbf{k}_s \mathbf{e}_y + \delta w \mathbf{k}_s \mathbf{e}_z.\end{aligned}\quad (23.19)$$

When the images are sheared in the  $x$ -direction, (23.19) is represented by

$$\Delta_x = \delta x \left( \frac{\delta u}{\delta x} \mathbf{k}_s \mathbf{e}_x + \frac{\delta v}{\delta x} \mathbf{k}_s \mathbf{e}_y + \frac{\delta w}{\delta x} \mathbf{k}_s \mathbf{e}_z \right), \quad (23.20)$$

where  $\delta x$  is the amount of shear in the  $x$ -direction on the object surface.

Similarly, for shearing in the  $y$ -direction, the relative phase change is

$$\Delta_y = \delta y \left( \frac{\delta u}{\delta y} \mathbf{k}_s \mathbf{e}_x + \frac{\delta v}{\delta y} \mathbf{k}_s \mathbf{e}_y + \frac{\delta w}{\delta y} \mathbf{k}_s \mathbf{e}_z \right), \quad (23.21)$$

where  $\delta y$  is the amount of shear in the  $y$ -direction on the object surface. For very small shears  $\delta x$  and  $\delta y$ , (23.20) and (23.21) can be rewritten as

$$\Delta_x = \delta x \left( \frac{\partial u}{\partial x} \mathbf{k}_s \mathbf{e}_x + \frac{\partial v}{\partial x} \mathbf{k}_s \mathbf{e}_y + \frac{\partial w}{\partial x} \mathbf{k}_s \mathbf{e}_z \right) \quad (23.22)$$

and

$$\Delta_y = \delta y \left( \frac{\partial u}{\partial y} \mathbf{k}_s \mathbf{e}_x + \frac{\partial v}{\partial y} \mathbf{k}_s \mathbf{e}_y + \frac{\partial w}{\partial y} \mathbf{k}_s \mathbf{e}_z \right). \quad (23.23)$$

Equations (23.22) and (23.23) are the fundamental equations for shearography and describe the whole-field correlation fringes as contours of constant first derivative of deformation instead of constant contours of deformation as in ESPI. For this reason, the shearogram depicts the strain concentrations directly and it is therefore suitable for nondestructive testing (NDT).

Equations (23.22) and (23.23) can be simplified by adjusting the direction of illumination. When the direction of illumination is in the  $x, z$ -plane, the sensitivity

vector lies in the  $x, z$ -plane as well. From Fig. 23.11 and (23.14) it follows that

$$\begin{aligned}\mathbf{k}_s \mathbf{e}_x &= |\mathbf{k}_s| \sin(\theta_{xz}/2) \\ &= (4\pi/\lambda) \cos(\theta_{xz}/2) \sin(\theta_{xz}/2) \\ &= (2\pi/\lambda) \sin \theta_{xz}, \\ \mathbf{k}_s \mathbf{e}_y &= 0, \quad \text{and} \\ \mathbf{k}_s \mathbf{e}_z &= |\mathbf{k}_s| \cos(\theta_{xz}/2) \\ &= (4\pi/\lambda) \cos(\theta_{xz}/2) \cos(\theta_{xz}/2) \\ &= (2\pi/\lambda)(1 + \cos \theta_{xz}).\end{aligned}$$

Given (23.22) and (23.23), it follows that

$$\begin{aligned}\Delta_x &= \delta x \left( \frac{\partial u}{\partial x} \mathbf{k}_s \mathbf{e}_x + \frac{\partial v}{\partial x} \mathbf{k}_s \mathbf{e}_y + \frac{\partial w}{\partial x} \mathbf{k}_s \mathbf{e}_z \right) \\ &= \frac{2\pi\delta x}{\lambda} \left[ \sin \theta_{xz} \frac{\partial u}{\partial x} + (1 + \cos \theta_{xz}) \frac{\partial w}{\partial x} \right],\end{aligned}\quad (23.24)$$

$$\begin{aligned}\Delta_y &= \delta y \left( \frac{\partial u}{\partial y} \mathbf{k}_s \mathbf{e}_x + \frac{\partial v}{\partial y} \mathbf{k}_s \mathbf{e}_y + \frac{\partial w}{\partial y} \mathbf{k}_s \mathbf{e}_z \right) \\ &= \frac{2\pi\delta y}{\lambda} \left[ \sin \theta_{xz} \frac{\partial u}{\partial y} + (1 + \cos \theta_{xz}) \frac{\partial w}{\partial y} \right].\end{aligned}\quad (23.25)$$

Similarly, when the direction of illumination is in the  $y, z$ -plane, the resulting equations are

$$\Delta_x = \frac{2\pi\delta x}{\lambda} \left[ \sin \theta_{yz} \frac{\partial u}{\partial x} + (1 + \cos \theta_{yz}) \frac{\partial w}{\partial x} \right], \quad (23.26)$$

$$\Delta_y = \frac{2\pi\delta y}{\lambda} \left[ \sin \theta_{yz} \frac{\partial v}{\partial y} + (1 + \cos \theta_{yz}) \frac{\partial w}{\partial y} \right]. \quad (23.27)$$

In these equations the illumination angles are characterized by  $\theta_{xz}$  or  $\theta_{yz}$ , and the shearing displacements by  $\Delta_x$  or  $\Delta_y$ . As shown in (23.24)–(23.27) a shearogram usually contains the in-plane as well as the out-of-plane terms of the strain tensor. When the illumination direction is adjusted normal to the object surface, the angle of illumination  $\theta$  becomes zero; thus  $\sin \theta = 0$  and  $\cos \theta = 1$ . The out-of-plane components  $\partial w/\partial x$  and  $\partial w/\partial y$  can be obtained from the following equations:

$$\Delta_x = \frac{4\pi\delta x}{\lambda} \frac{\partial w}{\partial x}, \quad (23.28)$$

$$\Delta_y = \frac{4\pi\delta y}{\lambda} \frac{\partial w}{\partial y}. \quad (23.29)$$

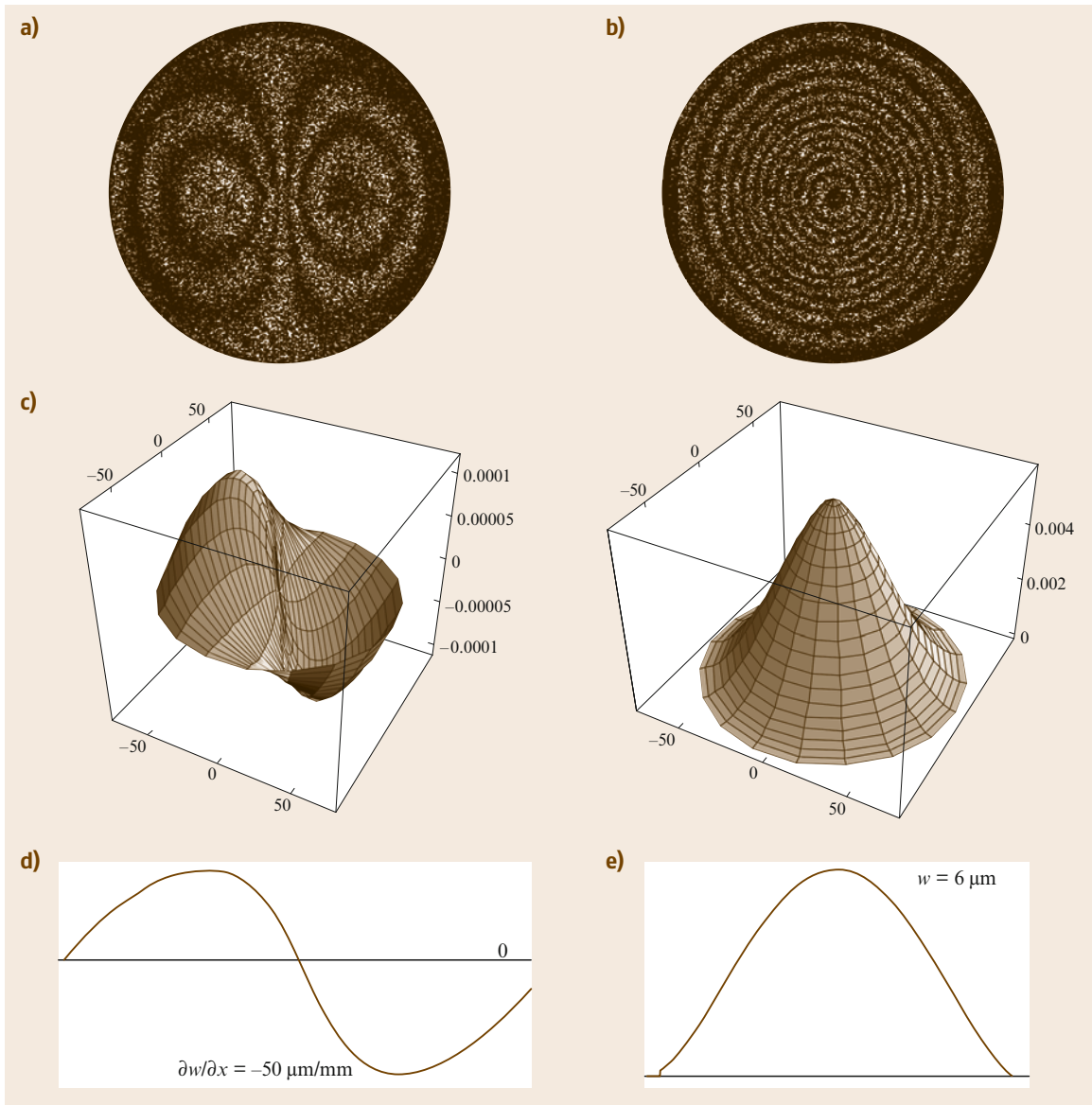


**Fig. 23.15a–e** Comparison shearography and ESPI for measuring the same out-of-plane deformation. (a) A shearogram, (b) a ESPI interferogram (c) evaluated shearogram and ESPI interferogram in 3-D view, (d) sectional plane  $\partial w/\partial x$ , (e)  $w$

To demonstrate the differences between the characteristic fringe pattern of digital shearography and that of ESPI, a circumferentially fixed circular aluminium plate, with a diameter of 150 mm and a thickness of 3 mm, was evaluated under the same loading condition by means of both speckle interferometric methods. Figure 23.15 shows the comparison of the results.

### 23.2.4 Quantitative Evaluation (SI)

Relative phase change can be determined numerically from a single fringe pattern by various methods of fringe analysis such as fringe tracking and Fourier transformation. However, these methods can not be automated due to the unavoidable need for human–computer interaction. The phase-shifting technique

introduces the possibility of automatic evaluation. Actually, relative phase change between two states can be calculated directly by using  $\Delta = \phi - \phi'$ , when the phase distributions  $\phi$  and  $\phi'$  are calculated by applying the phase-shifting technique. The phase distribution  $\phi$  is the first state of loading (no load or preload) of the object. The phase distribution  $\phi'$  corresponds to the second state of loading (or the second state of deformation).

Different methods of phase shifting can be applied for determining the phase distribution of an object state numerically and automatically. These methods can generally be divided into two categories: time-dependent (temporal) and spatial phase-shifting techniques. The temporal phase-shifting method is the most powerful technique for determining the phase distribution. With this method,  $N$  ( $N \geq 3$ ) frames of the same deformation state are stored sequentially to obtain a solvable system of equations consisting of three unknowns.

With the phase-shifting technique, however, a single frame is sufficient to determine the phase distribution. Thus, phase-shifting can be applied for vibration analysis, especially for measuring transient processes with a double-pulse laser. It is important to note that the determination of phase distribution by this technique is not as accurate as with the temporal method.

#### Temporal Phase Shifting (TPS)

Phase shifting can be executed by a wedge-shaped or parallel glass plate in front of a camera lens by moving a mirror a predetermined amount in the reference beam of an ESPI arrangement (Fig. 23.8) or by moving mirror 1 by using a piezoelectric transducer (PZT) in the digital shearographic setup (Fig. 23.13). By means of a diffraction grating or a liquid-crystal cell the phase shifting technique can also be realized without the mechanical movement.

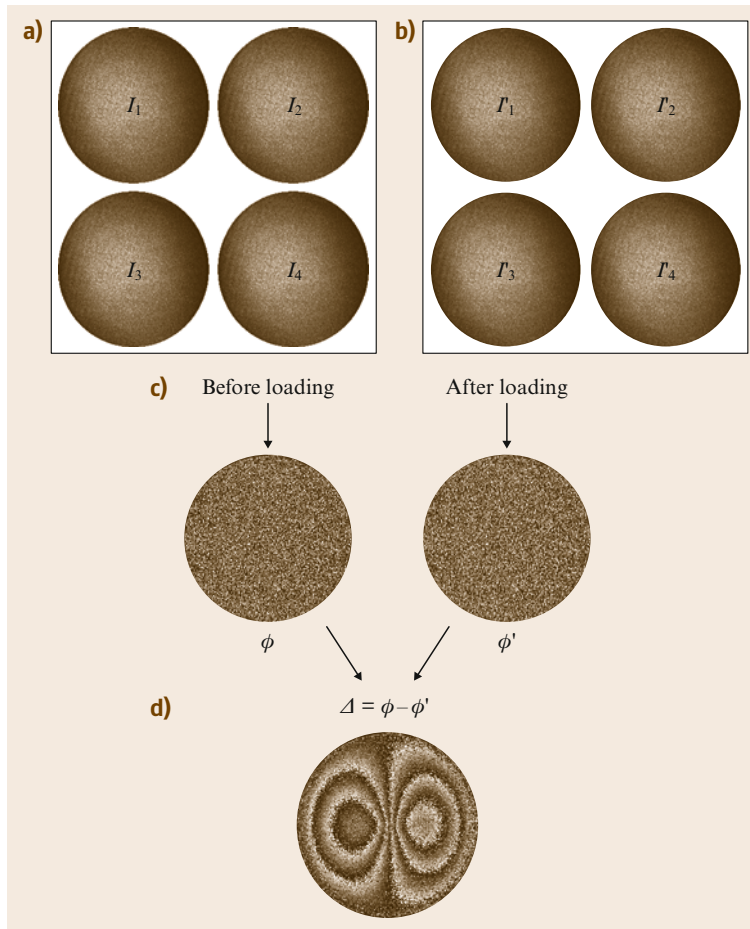


**Fig. 23.16** (a) Four stored intensity distributions  $I_1$  to  $I_4$ , and the calculated phase value  $\phi$  of the undeformed or preloaded state. (b) Four stored intensity distributions  $I'_1$  to  $I'_4$  and the calculated phase value  $\phi'$  of the deformed or second loaded state. (c) The phase distribution  $\phi$  and  $\phi'$  as a result of the measured intensities. (d) The phase map of the relative phase change  $\Delta$  obtained by digital subtraction of  $\phi'$  from  $\phi$

In temporal phase-shifting speckle interferometry, the measured intensity of a point  $P(x, y)$  on the object surface as recorded on the image plane of an optical system is given by

$$I_i(x, y, t_i) = I_0(x, y) \{ 1 + \gamma(x, y) \cos[\phi(x, y) + \phi_i(t_i)] \}, \quad i = 1, \dots, N, \quad (23.30)$$

where  $\phi(x, y)$  is the random phase of interest and  $\phi_i(x, y)$  is the additional phase shift in the  $i$ -th frame. There are three unknowns,  $\phi(x, y)$ ,  $I_0(x, y)$ , and  $\gamma(x, y)$ , in (23.30). Therefore, three or more equations are required to solve for the phase value  $\phi(x, y)$  when the phase shift  $\phi_i(x, y)$  is known. Most of the algorithms assume a known phase shift. However, the phase shift can also be an unknown.

In cases with  $N > 3$ , the phase value  $\phi(x, y)$  is overdetermined. However, experimental investigations have demonstrated that, in these cases, the measurement process is less sensitive to phase shifting if calibration errors are present.

Numerous algorithms have been developed over the last two decades for various applications. In most of the experiments where phase-shifting speckle interferometry is used, the so-called four-step algorithm [23.16] is usually applied. For this approach, four intensity speckle patterns are recorded to determine the experimental value of the phase shift  $\phi(x, y)$ . Using this technique, four phase shifts  $\phi_i(x, y)$  with  $i = 1, \dots, 4$ , (i. e.,  $\phi_1(x, y) = 0^\circ$ ,  $\phi_2(x, y) = 90^\circ$ ,  $\phi_3(x, y) = 180^\circ$ , and  $\phi_4(x, y) = 270^\circ$ ) are introduced so that an equation system of order four can be solved by

$$\phi(x, y) = \arctan \frac{I_4(x, y) - I_2(x, y)}{I_3(x, y) - I_1(x, y)}. \quad (23.31)$$

The same procedure is followed when the object is loaded with the following phase distribution of the alternate state of the object:

$$\phi'(x, y) = \arctan \frac{I'_4(x, y) - I'_2(x, y)}{I'_3(x, y) - I'_1(x, y)}. \quad (23.32)$$

Since the phase distributions  $\phi(x, y)$  and  $\phi'(x, y)$  are calculated in modulo  $2\pi$ , the relative phase difference  $\Delta = \phi - \phi'$  can be determined easily. The procedure is illustrated in Fig. 23.16.

### Spatial Phase Shifting (SPS)

An alternative phase-shifting technique is spatial phase shifting (SPS). Instead of the three or more exposures that are required in TPS for calculating the phase distribution of each object state, only a single frame is

required in SPS. In SPS, the phase distribution can either be encoded by a spatial carrier frequency on one image plane or be recorded by separate cameras with an appropriate static phase shift for each image. The first approach is attractive, because it does not require expensive optics, unlike the second approach.

When two wavefronts with a small angle interfere on a CCD chip, a linear phase change is generated from one pixel to another. Thus, a spatial carrier frequency can be introduced in SI by tilting the mirror M in the Michelson interferometer (Fig. 23.8). The tilting angle should be adjusted so that three to five pixels on the sensor correspond to a carrier period. The mean speckle size in the carrier direction, which can be changed by turning the aperture size in the imaging system, must be about three to five pixels to assure sufficient spatial correlation [23.17, 18]. Therefore, one single speckle should cover at least three to five supporting positions (pixels) in order to determine the phase relation. Various types of SPS methods and their theoretical descriptions are described in [23.19].

### Filtering and Unwrapping

The relative phase change determined by using phase-shifting technique is a noisy, sawtooth phase function exhibiting phase jumps of  $2\pi$  (modulo  $2\pi$ ). Such a phase map is the starting image for all the image processing procedures to follow. In image processing, a filter algorithm with modulo  $2\pi$  is first used since the phase fringe patterns show a low signal-to-noise ratio. Median or average filtering algorithms are frequently used in speckle interferometry.

Next, one-dimensional (1-D) and two-dimensional (2-D) demodulation of phase fringe patterns is performed (phase unwrapping); this consists of integrating or adding the phase values along a line or path. Each time the phase value jumps from zero to  $2\pi$ , the actual phase value is increased by  $2\pi$ . Similarly,  $2\pi$  is subtracted from the actual phase value when the phase value jumps from  $2\pi$  to zero.

The proper detection of the  $2\pi$ -phase jumps is an important issue during the demodulation of phase in an interferogram. For a filtered phase interferogram a simple demodulation algorithm (scanning the folded interferogram line by line and adding or subtracting  $2\pi$  for every phase jump) is sufficient as long as the phase values are continuously distributed over the entire image. D.W. Robinson gives the following summary of phase unwrapping-algorithms for path-dependent and path-independent methods:

Path-dependent phase demodulation algorithms:

- Sequential linear scanning
- Multiple scan directions
- Spiral scanning
- Counting around defects
- Pixel ordering/queuing

- Unwrapping by regions
- Tile processing

Path-independent phase demodulation algorithms:

- Cellular automata methods
- Band-limit approach (global feedback)

## 23.3 Applications

Speckle methods such as **ESPI**, digital shearography, and **DSC/DIC** discussed above, enjoy the advantages of being full-field noncontact methods. Therefore they have already been accepted by industry as a tool for nondestructive testing or evaluation (**NDT/NDE**), contour measurement, strain measurement, and vibration analysis, gaining more and more applications. The following applications have been measured by using digital shearography. More applications of **ESPI** and **DSC/DIC** are demonstrated in the chapters on *Holographic Interferometry* and *Digital Image Correlation* Chaps. 24 and 20.

### 23.3.1 NDT/NDE

The demands for greater quality and product reliability have created a need for better techniques of nondestructive testing (**NDT/NDI**), in particular, techniques for online inspection. Basically, we distinguish between three deformation processes that occur according to the nature of the loading: static, nonstationary (e.g., thermal, impact), and dynamic deformation processes.

#### Static Loading

In the case of static loading, the temporal phase-shifting method is always used. Four intensities are recorded during the constant maximum loading stage and four intensities in the minimum loading state, and the phase positions  $\phi$  and  $\phi'$  are calculated.

A cylinder of the kind actually used in conveying engineering for the transportation of paper and similar materials is described as an example. This roller basically consists of an outer rubber layer glued to a metal cylinder. During production, impurities on the metal surface can lead to partial delamination defects between the metal and the rubber.

In this application, the cylinder is evacuated in a vacuum chamber. The environmental pressure between the metal and the rubber in the area of the delaminations causes an out-of-plane deformation of

the rubber at those points where there is no bonding between the metal and the rubber. These deformations are visible in the phase image (Fig. 23.17). In order to detect possible disbands the cylinder should be scanned completely. Therefore, the cylinder has been divided into separate test areas. In every test area a test cycle according to the alternate loading and unloading is executed. From a segment of the cylinder a phase image recording  $\phi_1$  is made under loading  $p_{\max}$ , followed by a phase image recording  $\phi'_1$  in the unstressed state  $p_{\min}$ .

Then the cylinder and the camera are moved nearer to each other without altering the state of stress and a new testing area is set up. Without changing the load, a phase image recording  $\phi_2$  is made of the new test area and, following reloading, a further phase image recording  $\phi'_2$  is taken. It should be noted that this procedure saves one load change at every gauging.

#### Thermal Loading

Another type of deformation that is relatively difficult to control and which allows the deformation of the test specimen under investigation is thermal loading. Since the warming and cooling process is time dependent, the spatial phase-shifting technique is suitable for this kind of application.

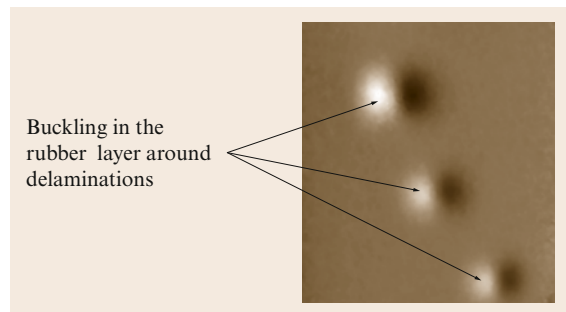


**Fig. 23.17** Demodulated phase image of a section of a conveying cylinder under vacuum

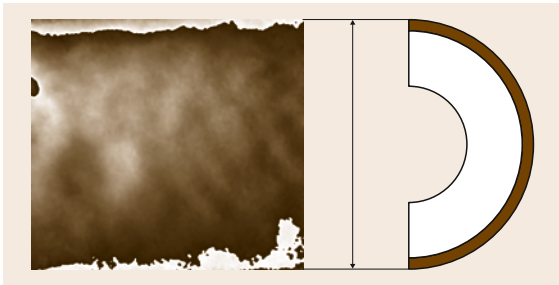


**Fig. 23.18** Cylinder segment without flaws

The task is to detect the delaminations and to make them visible using digital shearography. In the laboratory experiment the rubber layer is heated using a hot-air drier. The rubber is deformed relatively homogeneously with steady thermal loading and there is no areal expansion of the rubber where the lamination is intact.

The stationary radial expansion becomes noticeable in the phase image through a constant fringe or greyish distribution (Fig. 23.18). Only where the lamination is missing does the rubber layer show signs of bulging, due to the areal expansion of the rubber layer in view of the greater thermal expansion coefficient of rubber compared with steel to balance the different change of length with respect to the steel body. The bulging is interpreted as an area of disbond in the phase image (Fig. 23.19).

Figure 23.18 shows the longitudinal length of a cylinder without any signs of delamination. Figure 23.19 shows the longitudinal length of a cylinder displaying disbonding, visible in the form of buckling of the rubber layer in the phase map as a result of the thermal expansion.

#### Dynamic Loading

Damages and defects can be identified accurately under dynamic loading. Due to defects the regions of defects occur different stiffness, damping and therefore the different resonance frequencies as the entire structure. If the vibration mode can be observed or evaluated in real time, the defects can also be detected, when the test object is excited by a slow sine sweep. In order to map vibration mode, a recording technique allowing the real-time observation of the dynamic deformation of a tested specimen using the loading method is required. The recording technique that permits real-time observation synchronized with video is the *real-time subtraction* described in [23.20–26].

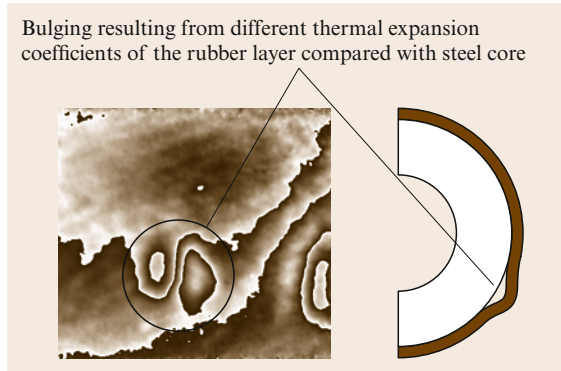


**Fig. 23.19** Cylinder segment with flaws

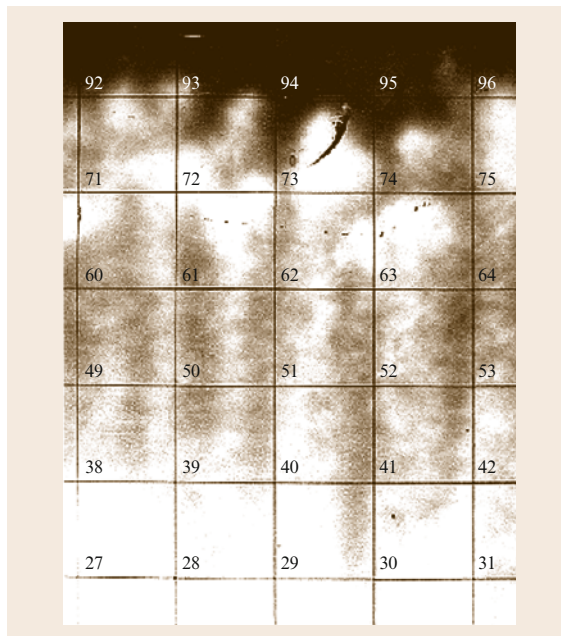


**Fig. 23.20** Honeycomb panel (size:  $1000 \times 1200 \times 12 \text{ mm}^3$ ) size of the grid:  $100 \times 100 \text{ mm}^2$

When the tested object vibrates in a stationary state at a frequency  $f$  that is higher than the video rate, the  $(n - 1)$ -th plotted image is a time-averaged shearogram recorded during a single video frame. The following  $n$ -th image is then digitally subtracted from the previous  $(n - 1)$ -th image i.e., the continuously renewed reference image technique. This makes the recording technique relatively insensitive to outside influences such as environmental disturbances using the continuous refreshment of the reference image. The result

is a simple time-averaged digital shearogram showing a fringe pattern that depends on the vibrating object. By using real-time subtraction with the continuously refreshed reference frame, the resonant frequencies of

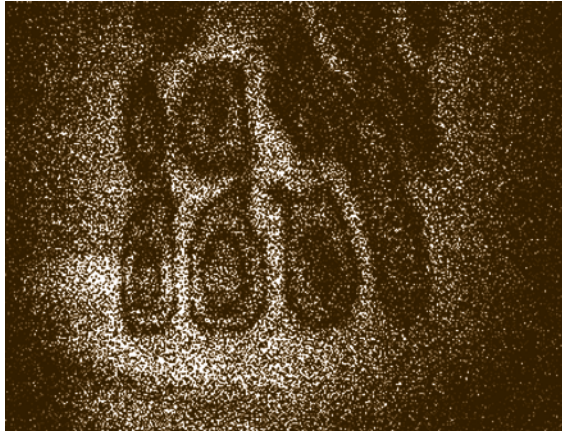


**Fig. 23.21** Time-averaged digital shearogram using real-time subtraction. The test object (Fig. 23.20) was excited by frequency  $f = 514$  Hz

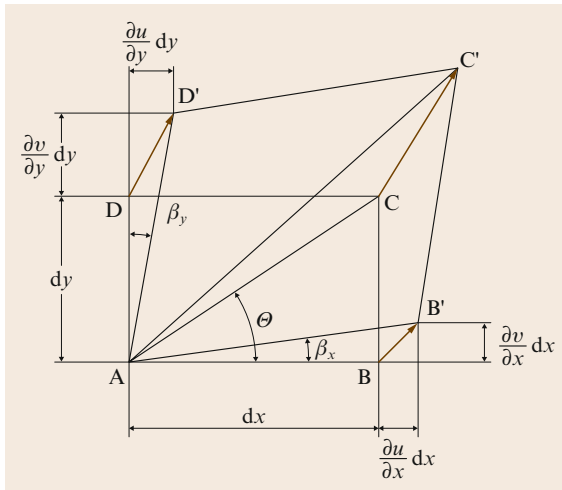


**Fig. 23.22** A small volume  $dx, dy, dz$  within a body is chosen to illustrate the deformation of the body area  $ABCD$  to  $AB'C'D'$

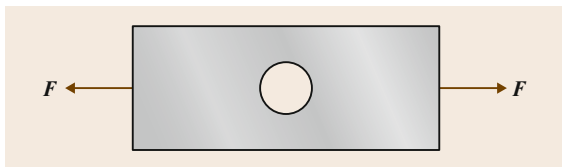


**Fig. 23.23** Araldite B tensile bar with a hole in the middle

the vibrating object (Fig. 23.20) as well as the natural frequency of the oscillating defect (Fig. 23.21) can be determined simply and rapidly.

### 23.3.2 Strain Measurement

Upon the deformation of a strained body, the displacement vector  $\mathbf{d}$  at an individual point can be split into the components  $u, v,$  and  $w$  in the  $x$ -,  $y$ -, and  $z$ -directions, respectively. Figure 23.22 shows the elastic deformations of a small solid rectangle. With the assumption of small angles, the shear strain can be expressed approximately by using the derivatives of the displacement components. Thus, three normal strains and three shear strains can be written as

$$\varepsilon_{xx} = \frac{\partial u}{\partial x}, \quad \varepsilon_{yy} = \frac{\partial v}{\partial y}, \quad \varepsilon_{zz} = \frac{\partial w}{\partial z}, \quad (23.33)$$

and

$$\begin{aligned} \gamma_{xy} &= \frac{\partial u}{\partial y} + \frac{\partial v}{\partial x}, & \gamma_{yz} &= \frac{\partial v}{\partial z} + \frac{\partial w}{\partial y}, \\ \gamma_{zx} &= \frac{\partial w}{\partial x} + \frac{\partial u}{\partial z}. \end{aligned} \quad (23.34)$$

Since usually only the surface of the tested object can be measured, no information can be obtained normal to the surface (or in the  $z$ -direction) of the object. The deformation gradient  $\partial u/\partial z, \partial v/\partial z, \partial w/\partial z$  cannot be measured directly. Only in a few cases can the out-of-plane strain  $\partial w/\partial z$  be calculated indirectly. For this reason it is possible to measure only the following six components directly:

$$\mathbf{H} = \begin{pmatrix} \frac{\partial u}{\partial x} & \frac{\partial u}{\partial y} \\ \frac{\partial v}{\partial x} & \frac{\partial v}{\partial y} \\ \frac{\partial w}{\partial x} & \frac{\partial w}{\partial y} \end{pmatrix}. \quad (23.35)$$

With (23.24)–(23.29) in Sect. 23.2.3, six components of the matrix  $\mathbf{H}$  can be generated by varying the illumination planes and shearing directions. An application of measuring in-plane strain and out-of-plane components solely using a tensile bar manufactured from Araldite B with a hole in the middle is shown in Fig. 23.23, and loaded to 136 N in Fig. 23.24a–g. Figure 23.24a and d show the fringe patterns of the in-plane strains  $\varepsilon_{xx}$  and  $\varepsilon_{yy}$ , while Fig. 23.24b,c show  $\partial u/\partial y$  and  $\partial v/\partial x$ . As an additional result, the out-of-plane deformation gradients  $\partial w/\partial x$  and  $\partial w/\partial y$  can be measured directly (Fig. 23.24e,f) and represented by their pseudo-3-D



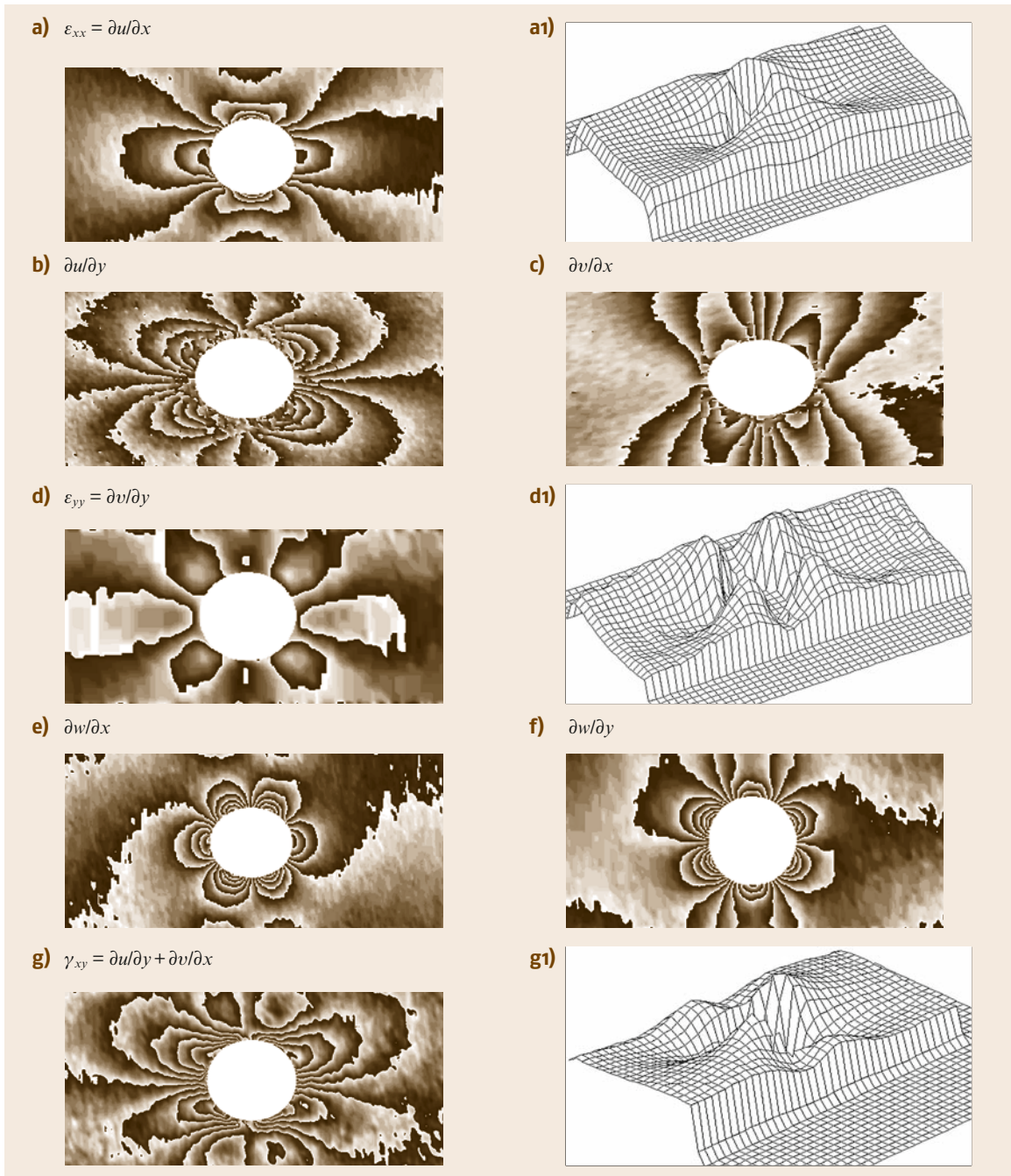


**Fig. 23.24a–g** Strain phase images for the bar shown in Fig. 23.23: (a)  $\partial u/\partial x$ , (b)  $\partial u/\partial y$ , (c)  $\partial v/\partial x$ , (d)  $\partial v/\partial y$ , (e)  $\partial w/\partial x$ , (f)  $\partial w/\partial y$ , and (g)  $\gamma_{xy} = \partial u/\partial y + \partial v/\partial x$ . (a1), (d1), (g1), corresponding 3-D plots

plots. The measurement results indicate that the out-of-plane strain components in the area near the hole are not

equal to zero, although the tensile bar is loaded under plane-stress conditions.

## 23.4 Bibliography

- J. W. Goodman: *Statistical Optics* (Wiley, New York 1985)
- C.M. Vest: *Holographic Interferometry* (Wiley, New York 1979)
- R.S. Sirohi (Ed.): *Speckle Metrology* (Marcel Dekker, New York 1993)
- T. Kreis: *Holographic Interferometry: Principles and Methods* (Akademie Verlag, Berlin 1996)
- K.P. Rastogi (Ed.): *Holographic Interferometry: Principles and Methods* (Springer, Berlin, Heidelberg 1994)
- W. Osten: *Digitale Verarbeitung und Auswertung von Interferenzbildern* (Akademie Verlag, Berlin 1991)
- R. Jones, C. Wykes: *Holographic and Speckle Interferometry* (Cambridge Univ. Press, Cambridge 1989) Chap. 2
- W. Steinchen, L.X. Yang: *Digital Shearography – Theory and Application of the Digital Speckle Pattern Shearing Interferometry* (SPIE, Washington 2003)
- P.K. Rastogi (Ed.): *Optical Measurement Techniques and Applications* (Artech House, Boston 1997)
- D.W. Robinson, G.T. Reid (Eds.): *Interferogram Analysis: Digital Fringe Pattern Measurement Analysis* (Institute of Physics, Bristol 1993)
- E. Hecht, A. Zajac: *Optics* (Addison-Wesley, Reading 2003)

## References

- 23.1 K. Exner: Über die Frauenhofer'schen ringe, die Quetelet'schen streifen und verwandte erscheinungen, Sitzungsberichte der Akademie der Wissenschaften Wien. **11**(76), 522–550 (1877)
- 23.2 P. Hariharan: Speckle patterns: A historical retrospect, *J. Modern Opt.* **19**(9), 791–793 (1972)
- 23.3 M. von Lauer: Die Beugungserscheinungen an vielen unregelmäßig verteilten teilchen, Sitzungsberichte der preussischen Akademie der Wissenschaften zu Berlin **47**, 1144–1163 (1914)
- 23.4 G. Groh: Proc. Engineering Uses of Holography, ed. by E.R. Robertson, J.M. Harvey (Cambridge Univ. Press, Cambridge 1970) pp. 483–494
- 23.5 J.W. Goodman: Statistical properties of laser speckle patterns. In: *Laser Speckle and Related Phenomena*, ed. by J.C. Dainty (Springer, New York 1975) pp. 9–75
- 23.6 J.W. Goodman: Some fundamental properties of speckle, *J. Opt. Soc. Am.* **66**(11), 1145–1150 (1976)
- 23.7 E.N. Leith, J. Upatnieks: Reconstructed wavefronts and communication theory, *J. Opt. Soc. Am.* **52**, 11232–1130 (1962)
- 23.8 J.N. Butters, J.A. Leendertz: Speckle pattern and holographic techniques in engineering metrology, *Opt. Laser Tech.* **3**, 36–30 (1971)
- 23.9 A.E. Ennos: Speckle Interferometry. In: *Laser Speckle and Related Phenomena*, ed. by J.C. Dainty (Springer, New York 1975) pp. 203–253
- 23.10 J.H. Tiziani: A study of the use of laser speckle to measure small tilts of optically rough surfaces accurately, *Opt. Commun.* **5**, 271–276 (1972)
- 23.11 J. M. Burch, J. M. J. Tokarski: Production of multiple beam fringes from photographic scatterers, *Opt. Acta* **15**(2) 101–111 (1968)
- 23.12 E. Archbold, A.E. Ennos: Displacement measurement from double-exposure laser photographs, *Opt. Acta* **19**(4), 253–271 (1972)
- 23.13 Th. Fricke-Begemann: Optical Measurement of Deformation Fields and Surface Processes with Digital Speckle Correlation, Dissertation. University of Oldenburg 2002
- 23.14 J.A. Leendertz, J.N. Butters: An image-shearing speckle-pattern interferometer for measuring bending moments, *J. Phys. E: Sci. Instrum.* **6**, 1107–1110 (1973)
- 23.15 Y.Y. Hung, R.E. Rowlands, I.M. Daniel: Speckle-shearing interferometric technique: a full-field strain gauge, *Appl. Opt.* **14**(3), 618–622 (1975)
- 23.16 K. Creath: Phase shifting speckle interferometry, *Appl. Opt.* **24**(18), 3053–3058 (1985)
- 23.17 J. Burke, H. Helmers: Performance of spatial versus temporal phase shifting in ESPI, *Proc. SPIE* **3744**, 188–199 (1999)
- 23.18 T. Bothe, J. Burke, H. Helmers: Spatial phase shifting in electronic speckle pattern interferometry: minimization of phase reconstruction errors, *Appl. Opt.* **36**(22), 5310–5316 (1997)
- 23.19 M. Kujawinska: Spatial phase measurement methods. In: *Interferogram Analysis, Digital Fringe Pattern Measurement*, ed. by D.W. Robinson, G.T. Reid (IOP, Bristol 1993)
- 23.20 W. Steinchen, L.X. Yang, G. Kupfer: Vibration analysis by digital shearography, *Proc. SPIE* **2868**, 426–437 (1996)
- 23.21 R.L. Powell, K.A. Stetson: Interferometric hologram evaluation and real-time vibration analysis of diffuse objects, *J. Opt. Soc. Am.* **55**, 1694–1695 (1965)

- 23.22 R.L. Powell, K.A. Stetson: Interferometric vibration analysis of 3-D-objects by wavefront reconstruction, *J. Opt. Soc. Am.* **55**, 1593–1598 (1965)
- 23.23 J.D.R. Valera, O.J. Løkberg: Composite vibration analysis with modulated electronic speckle shearing interferometry, *Opt. Rev.* **4**(2), 261–264 (1997)
- 23.24 J.D.R. Valera, J.D.C. Jones, O.J. Løkberg: Exact vibration amplitude derivative measurement with TV shearography, *Meas. Sci. Technol.* **7**, 918–921 (1966)
- 23.25 W. Steinchen, Y. Gan, G. Kupfer, P. Mäckel: Digital shearography using stroboscopic illumination additional to time average method, 6-th AIVELA-Conference (Ancona 2004)
- 23.26 W. Steinchen, Y. Gan, G. Kupfer: Comparison of vibration measurements – Laser Doppler Vibrometry and Digital Shearography, Workshop for final meeting LAVINYA (Ancona, 2005)